Quantitative evaluation of orientation-specific damage using elastic waves and probability-based diagnostic imaging

Chao Zhou, Zhongqing Su, Li Cheng *

The Department of Mechanical Engineering, The Hong Kong Polytechnic University, Kowloon, Hong Kong Special Administrative Region

ARTICLE INFO

ABSTRACT

Different from the damage with relatively smooth boundaries or edges such as a through-thickness hole or delamination which scatters elastic waves omnidirectionally, orientation-specific damage of sizable length in a particular dimension (e.g., a crack or a notch) often exerts strong directivity to elastic wave propagation. As a consequence the damage-scattered waves may not be captured efficiently by sensors at certain locations, posing a challenging issue to elastic-wave-based damage identification. In this study, the influence of damage orientation on Lamb wave propagation was quantitatively scrutinised. Based on the established correlation between damage parameters (location, orientation, shape and size) and extracted signal features, a probability-based diag- nostic imaging approach was developed, in conjunction with use of an active sensor network in conformity to a pulse–echo configuration. Relying on enhancive signal features including both the temporal information and signal intensity, this imaging approach is capable of indicating the orientation of individual damage edges clearly and further shape/size of the damage. The effectiveness of the approach was demonstrated by predicting orientation-specific damage cases including a triangular through-thick- ness hole (through finite element simulation), a through-thickness crack and an L-shape crack (through experiment) in aluminium plates. With the assistance of a two-level synthetic image fusion scheme, all damage cases were visually and quantitatively highlighted in the probability images.

© 2011 Elsevier Ltd. All rights reserved.

1. Introduction

Structural health monitoring (SHM) involves a paradigm of sensor selection and allocation, signal activation and sensing, data feature extraction and fusion, as a means of appropriately assessing the health conditions of a structure under the monitoring. In the past two decades there has been increasing awareness of introducing SHM to various industrial sectors. Successful implementation of such a technique can substantially enhance operational efficiency of an engineering system, drive down exorbitant maintenance costs and prolongate its lifespan. Amongst different SHM techniques, those based on the mechanism of the interaction between elastic waves and structural damage present many advantages over the others in terms of resolution, practicality and detectability. Of particular interests are Lamb waves, the modality of elastic waves confined in thin sheet-like structures (with planar dimensions being far greater than that of the thickness and with the wavelength being of the order of the sheet thickness). With features including strong penetration,

---

* Corresponding author. Fax: +852 2365 4703.
    E-mail address: MMLCHENG@polyu.edu.hk (L. Cheng).

fast propagation, <mark>omnidirectional</mark> dissemination and high sensitivity to defects/flaws/damage in their propagation paths, Lamb waves have been intensively employed to develop various SHM techniques [1–11].

However, when dealing <mark>with the orientation-specific or sharp-angled damage</mark> featuring a dominant size in a particular dimension (e.g., a crack or a notch), a challenging issue is that such sort of damage often exerts strong directivity to wave propagation. It is largely different from the damage with relatively smooth boundaries or edges such as a through-thickness hole or delamination, which scatters elastic waves omnidirectionally. As a result, information associated with the damage may not be efficiently extracted from signals captured by sensors at certain locations, in the absence of prior knowledge of damage orientation or shape. Further down to a fine level, the periphery of structural damage such as delamination can be described as the continuum of a number of cracks with various lengths which shape the damage, although macroscopically the damage presents relatively smooth boundaries. This implies ascertainment of the orientation and length of individual cracks can facilitate a quantitative depiction of damage shape. Allowing for this consideration, it is of necessity to calibrate the influence of damage orientation on elastic wave propagation, a prerequisite to develop a quantitative elastic-wave-based damage identification approach for damage of arbitrary shape.

Some studies have been carried out to address this issue. Representatively, Lowe et al. [12] and Lowe and Diligent [13] examined the reflection of fundamental Lamb wave modes from surface-breaking rectangular notches with different widths and depths, in which an approach based on both the low- and high-frequency asymptotic analyses was used to investigate behaviours of reflected waves. Ihn and Chang [14] developed a built-in diagnostic technique for monitoring fatigue crack growth. Tua et al. [15] contributed a method to evaluate crack length by observing the strength of crack-scattered wave signals. Lu et al. [16] explored the effect of crack orientation on wave propagation and assessed the crack in terms of reflection and transmission coefficients. Chang and Mal [17] proposed a specialised finite element (FE) method and an experimental technique to interrogate Lamb waves scattered from a circular hole with edge cracks. Notwithstanding quantitative evaluation of orientation-specific damage yet remains challenging.

On the other hand, the probability-based diagnostic imaging, an emerging SHM and damage identification technique, has been attracting a great deal of attention in recent years [18–20]. Such an approach attempts to describe the structural
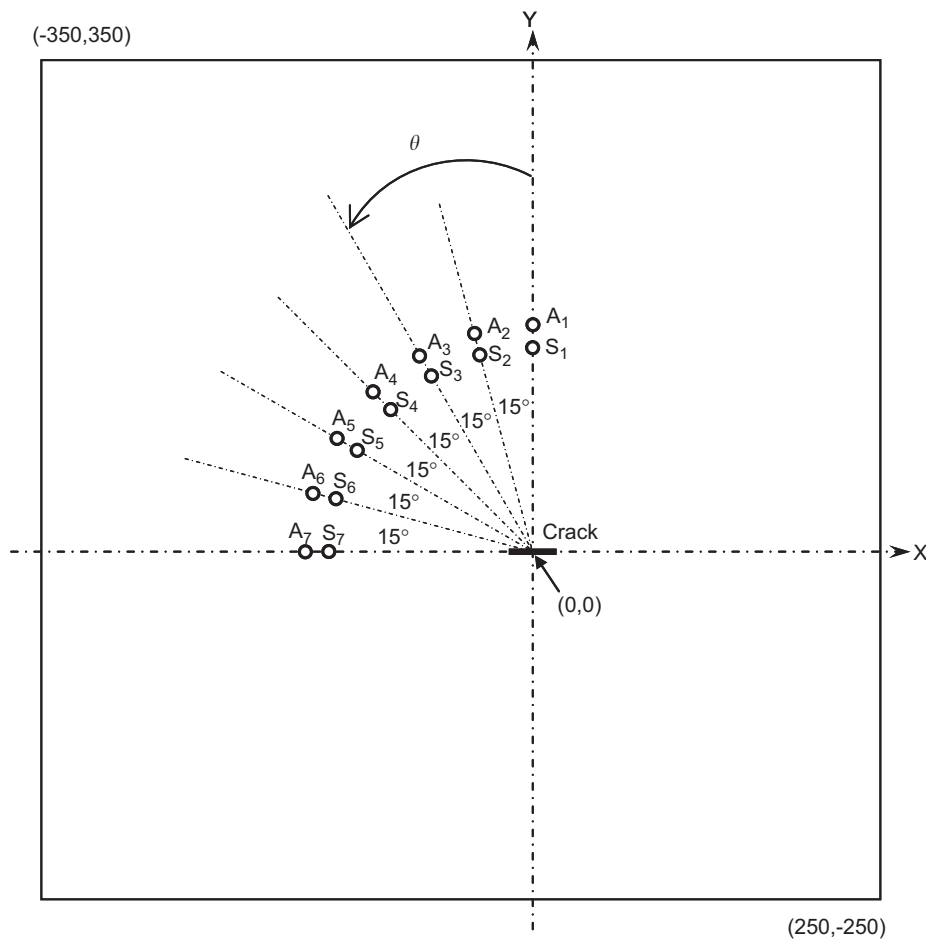

Fig. 1. An aluminium plate bearing a through-thickness crack and seven actuator–sensor pairs in conformity to pulse–echo configuration (unit: mm).

health status or a damage event using an easily interpretable image whose pixels exclusively correspond to spatial points of the structure under inspection. The field value of a pixel stands for the probability of damage presence at the point of the structure corresponding to this pixel, and the degree of probability is often calibrated by different grey scales. It is appreciated that presenting damage identification results in terms of the probability is an improvement over traditional identification techniques which have an ultimate goal to define damage with deterministic parameters (e.g., location coordinates, size or length), because the underlying concept of 'probability' is more consistent with the implication of 'prediction' or 'estimation' of damage. Nevertheless it is envisaged that majority of the currently existing probability-based diagnostic imaging approaches, substantially based on canvassing changes in temporal information such as time-of-flights (ToFs) extracted from captured wave signals, fail to portray damage quantitatively including its orientation, shape and size, because difference in damage orientation, shape and size would not lead to pronounced changes in ToFs.

It is the above-addressed deficiencies of current SHM techniques that have motivated the present study. Effect of the orientation of damage with sizable length in a particular dimension (orientation-specific damage) on Lamb wave propagation was scrutinised. Based on two established correlations between (1) damage location and ToFs extracted from signals and (2) intensity of signal energy scattered by damage and damage orientation, an enhanced probability-based diagnostic imaging method was developed. With the assistance of an active sensor network in conformity to a pulse–echo configuration and a two-level synthetic image fusion scheme, structural damage can visually be highlighted in a probability image, including a clear indication of its orientation and shape. The effectiveness of this approach was demonstrated by predicting typical orientation-specific damage including a triangular through-thickness hole (through FE simulation), a through-thickness crack and an L-shape crack (through experiment).

2. Influence of damage orientation on Lamb wave propagation

To qualitatively investigate and calibrate the influence of damage orientation on Lamb wave propagation, both FE simulation and experimental validation were carried out.
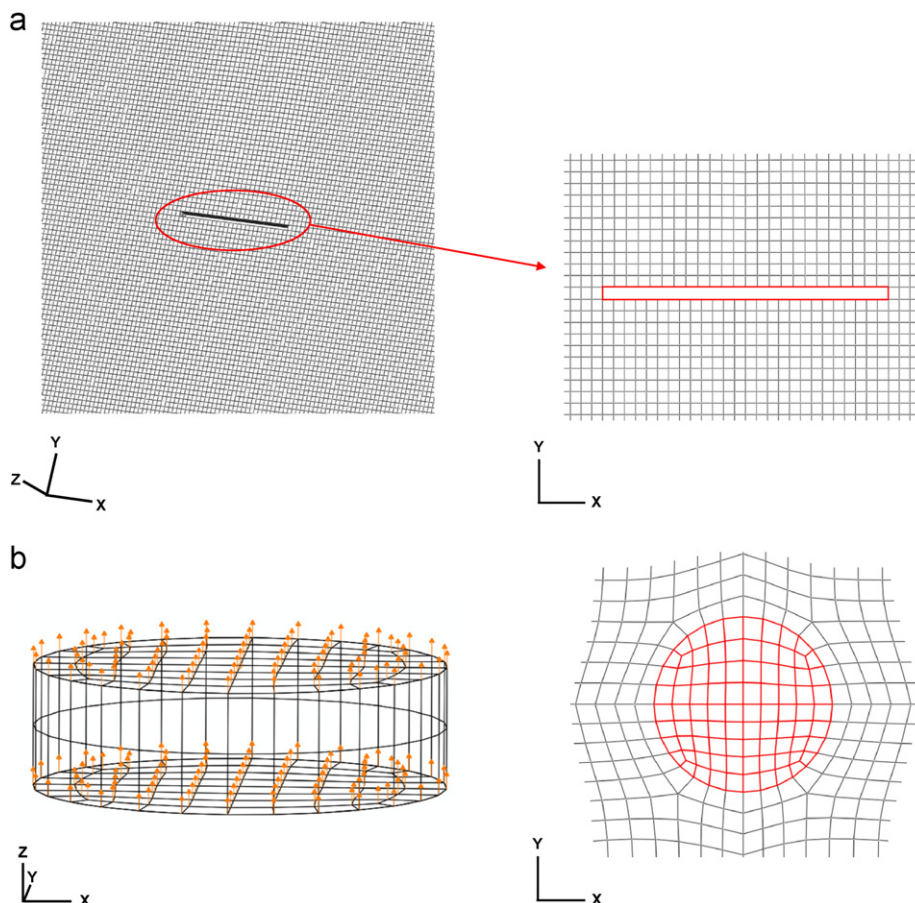

Fig. 2. (a) Partial FE model of the aluminium plate in Fig. 1 with zoomed-in part containing a through-thickness crack and (b) PZT actuator model (left: profile view, right: top view) with imposed out-of-plane (z-axis) displacement constraints for generating the A_0 mode dominating overall signal energy.

2.1. FE simulation

A thin aluminium plate measuring $600 \times 600 \times 1.5$ mm^3 with encastre boundary conditions as shown schematically in Fig. 1 was considered. A through-thickness crack, 16 mm long and 0.64 mm wide, was assumed in the plate in parallel with the lower edge of the plate, with its centre being 250 mm away from the lower and right edges of the plate. Fourteen circular piezoelectric lead zirconate titanate (PZT) elements, 5 mm in diameter each, were allocated on the plate as seen in Fig. 1, half of which served as wave actuators to generate elastic waves, denoted by A_i $(i = 1, 2, \ldots, 7)$ in what follows, while the rest as sensors to capture wave signals reflected from the crack, denoted by S_i $(i = 1, 2, \ldots, 7)$. Each PZT actuator, A_i, and its contiguous sensor, S_i (the one located on the line connecting A_i and crack centre) were 7 mm apart from each other, forming an actuator–sensor pair (or a sensing path) in line with a pulse–echo configuration, denoted by $A_i - S_i$. Featuring the same distance of 100 mm between the actuator and crack centre, these seven sensing paths provided seven different angles of wave incidence (θ) relative to the crack orientation, varying from 0^0 to 90^0 with an increment of 15^0. Both symmetric and anti-symmetric Lamb modes can be employed for damage detection [21], while in this study, the lowest-order anti-symmetric mode, A_0, was preferred because it, in comparison with its symmetric counterpart, S_0, has (i) a shorter wavelength at a given frequency and therefore higher sensitivity to damage of smaller size and (ii) larger signal magnitude, giving a signal with high signal-to-noise ratio (SNR).

In the simulation, the plate was modelled using three-dimensional eight-node brick elements, and the crack was formed by removing associated FE elements, in Fig. 2(a). The A_0 mode was activated using five-cycle *Hanning*-window-modulated sinusoid tonebursts at a central frequency of 450 kHz as the incident wave. This frequency is lower than the cut-off thresholds of higher-order Lamb modes in the discussed plate, to avoid occurrence of multiple modes. To ensure the dominance of the A_0 mode in signal energy, uniform out-of-plane (z-axis) displacement constraints were applied on FE nodes of the upper and lower surfaces of the PZT actuator model, as shown in Fig. 2(b), in recognition of the fact that A_0 is dominated by the out-of-plane displacement of particles. Simulation was carried out using ABAQUS®/EXPLICIT.
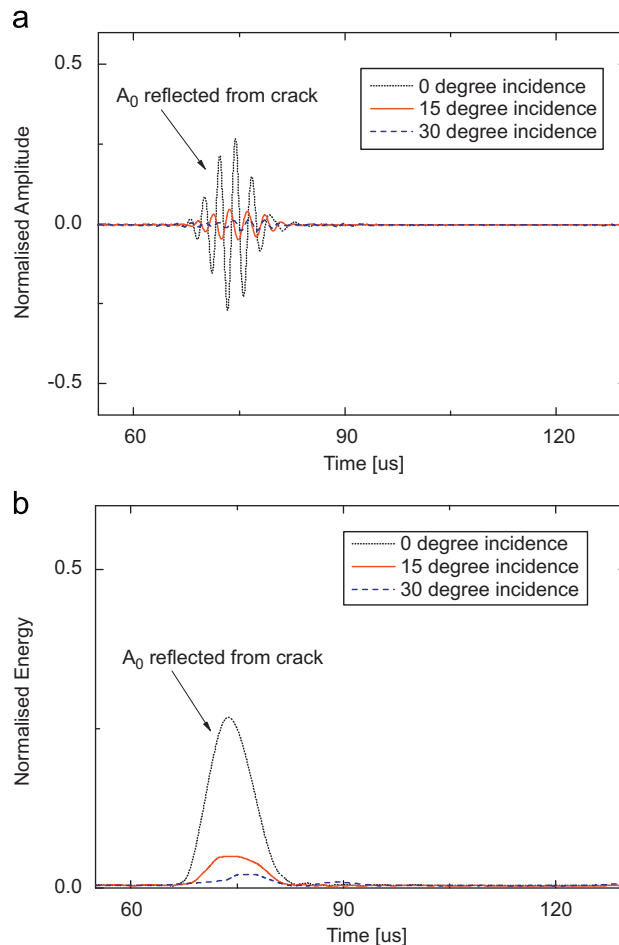

Fig. 3. (a) Crack-reflected A_0 modes (residual signals) acquired via sensing paths $A_1 - S_1$ $(\theta = 0^0)$, $A_2 - S_2$ $(\theta = 15^0)$ and $A_3 - S_3$ $(\theta = 30^0)$ from FE simulation (showing signal fragments containing damage-reflected A_0 mode only; normalised by the magnitude of corresponding incident waves) and (b) envelopes of energy distribution of signals in (a) obtained using HT-based signal processing.

The crack-reflected wave signals were captured by calculating the strains at places where sensors were located. To ensure accuracy, the largest dimension of FE elements was 0.67 mm, guaranteeing that ten elements were allocated per wavelength of A_0.   crack-reflected signals = current signals - baseline signals

As typical simulation results, crack-reflected wave signals, the residual signals upon subtracting corresponding baseline signals (those acquired via the same sensing paths in the same structure without simulated crack) from current signals, acquired via three representative sensing paths, A_i-S_i ($i = 1,2,3$; i.e., $\theta = 0^0$, $\theta = 15^0$ and $\theta = 30^0$, respectively), are displayed in Fig. 3(a). All the captured signals were normalised relative to the magnitude of their corresponding incident waves, and then applied with a Hilbert transform (HT)-based signal processing [22], so as to depict energy distribution of signals, shown in Fig. 3(b). In HT-processed signals, peak values of the envelope of energy distribution were set as the energy intensities of individual wave packets. Taking into account seven sensing paths, a correlation between the intensity of crack-reflected wave energy and angle of wave incidence relative to the crack orientation was obtained, as shown in Fig. 4. It can be seen that the strongest reflection from crack was captured via A_1-S_1 (normal incidence, $\theta = 0^0$); with the increase of incidence angle, the intensity of crack-reflected energy decreases monotonously and reaches its minimum when $\theta = 90^0$; and remarkable decrease takes when $\theta < 30^0$, whereas no significant decrease can further be observed when $\theta > 30^0$.

To further explore the effect of crack length on the above established correlation, the crack length was varied from 10 to 30 mm with an increment of 2 mm. The linkages between the intensity of crack-reflected wave energy and angle of wave incidence are exhibited in Fig. 5 for several representative lengths, to observe that, at a given angle of incidence, the intensity of wave energy reflected by a longer crack is slightly stronger than that by a shorter crack, although certain fluctuation of such a trend can be noticed. However the discrepancy due to crack length in the discussed variation range (10–30 mm, i.e., 1.5–4.5 times the wavelength of the selected A_0 mode) is insignificant and would not lead to evident difference in established correlations.
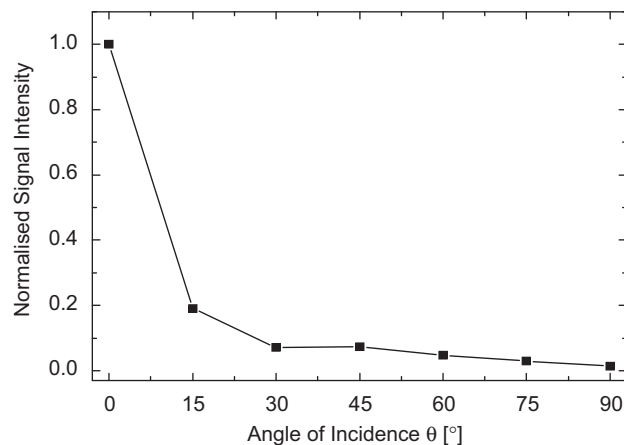

Fig. 4. Intensity of signal energy reflected by a crack vs. angle of wave incidence from FE simulation.
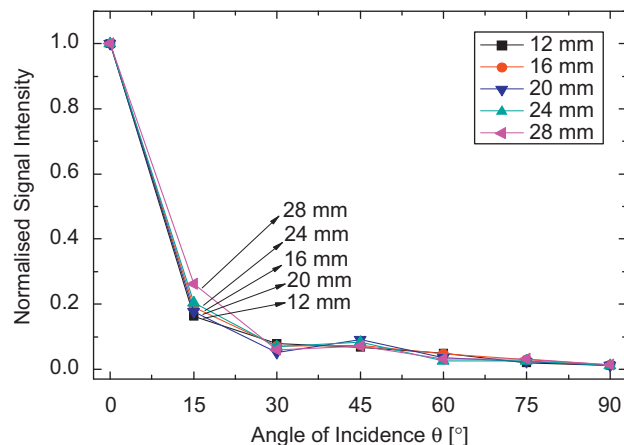

Fig. 5. Intensity of signal energy reflected by cracks of different lengths vs. angle of wave incidence from FE simulation.

2.2. Experimental validation

Experiments were conducted to validate the above FE simulation using the same configurations. Material properties and geometry of the PZT wafers used are detailed in Table 1. All actuator-sensor pairs in the sensor network were instrumented with a signal generation and acquisition system developed on a *VXI* platform [23], shown in Fig. 6. The 16 mm long through-thickness crack was introduced to the aluminium plate using a fine blade (0.64 mm wide). The excitation signal, same as the one used in simulation, was generated by a waveform generator (Agilent® E1441) and amplified using a linear signal amplifier (PiezoSys® EPA-104) to 60 V_{p-p}, which was then applied on each PZT actuator in turn to activate the A_0 mode dominating overall signal energy. The crack-reflected waves were acquired via each sensing path using an oscilloscope (HP^{TM}-54810A) at a sampling rate of 25 MHz.

As typical results of experiment, crack-reflected wave signals, the residual signals upon subtracting corresponding baseline signals from current signals, acquired via three representative sensing paths, A_i-S_i ($i = 1, 2, 3$; i.e., $\theta = 0^0$, $\theta = 15^0$ and $\theta = 30^0$, respectively), are exhibited in Fig. 7, together with their corresponding HT-processed counterparts. Similarly, dependence of the intensity of crack-reflected wave energy on the angle of wave incidence was ascertained, plotted in Fig. 8. Results from experiment (Figs. 7 and 8) can be seen to match well those from simulation (Figs. 3 and 4), showing consistent correlation between scattering characteristics of the crack-reflected A_0 wave mode and angle of wave incidence (Figs. 4 and 8).

To further investigate the influence of excitation frequency on the above established relationship, the experiment was repeated in a sweep frequency range from 350 to 550 kHz with an increment of 50 kHz. The accordingly obtained linkages between the intensity of crack-reflected wave energy and angle of wave incidence are shown in Fig. 9 for representative frequencies, to observe that, at a given angle of incidence, the intensity of crack-reflected wave at a higher frequency is slightly weaker than that reflected by the same crack but at a lower frequency. This can be attributed to the fact that elastic waves at higher frequencies possess shorter wavelengths, presenting higher sensitivity to variation in angle of wave

Table 1
Material and geometric properties of PZT wafer used in active sensor network.

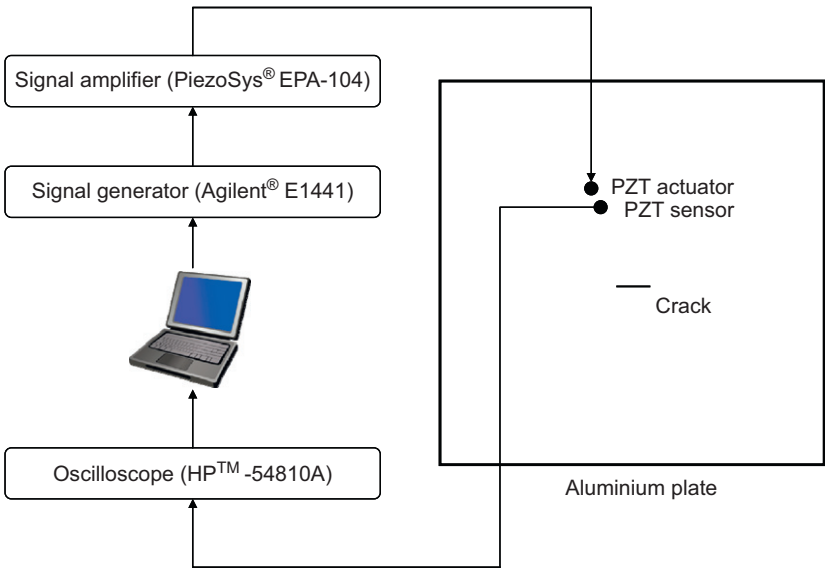| Product name	PI 151
Diameter	5 mm
Thickness	0.5 mm
Density	7.80 g/cm^3
Poisson's ratio	0.31
Charge constant d_{31}	-170×10^{-12} m/V
Charge constant d_{33}	450×10^{-12} m/V
Relative dielectric constant	1280
Dielectric permittivity p_0	8.85×10^{-12} F m^{-1}
Young's modulus E	66 GPa

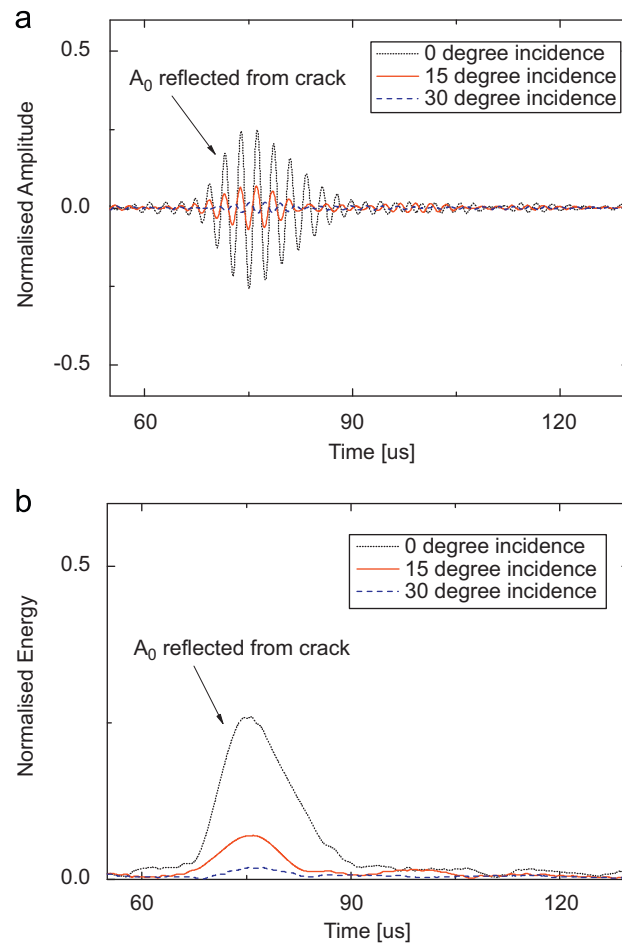
Fig. 6. Schematic of experiment set-up.

Fig. 7. (a) Crack-reflected A_0 modes (residual signals) acquired via sensing paths A_1-S_1 ($\theta = 0^0$), A_2-S_2 ($\theta = 15^0$) and A_3-S_3 ($\theta = 30^0$) from experiment (showing signal fragments containing damage-reflected A_0 mode only; normalised by the magnitude of corresponding incident waves) and (b) envelopes of energy distribution of signals in (a) obtained using HT-based signal processing.
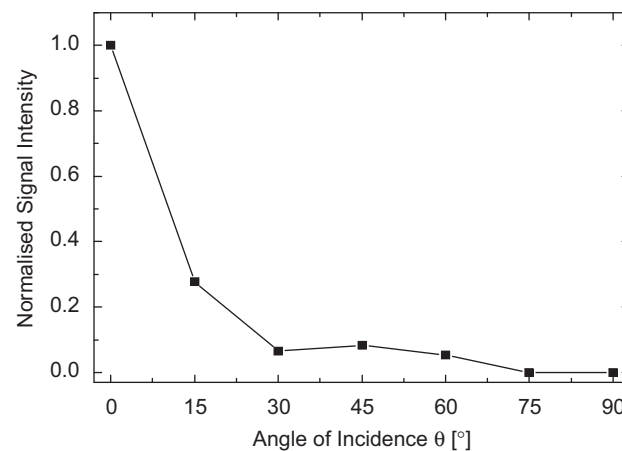

Fig. 8. Intensity of signal energy reflected by a crack vs. angle of wave incidence from experiment.

incidence and leading to more changes in signal energy. Although this observation implies that different correlations between reflected energy and wave incidence angle should be selected in terms of the wave frequency, the diversity in the discussed range (350–550 kHz) is not pronounced.
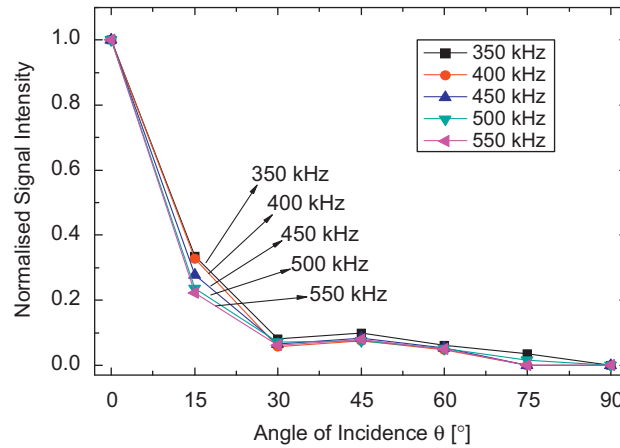
Fig. 9. Intensity of signal energy reflected by a crack at different excitation frequencies vs. angle of wave incidence from experiment.

3. Compensation for wave attenuation

The intensity of damage-scattered wave energy changes subject to not only the orientation of damage as discussed previously, but also the propagation distance, a phenomenon known as *wave attenuation*. In order to evaluate damage orientation according to changes in signal intensity described by Figs. 4 and 8, it is of vital necessity to compensate for variation in the intensity due to wave attenuation, whereby changes in signal intensity, if any, can solely be attributed to damage orientation. Basically wave attenuation with propagation distance can be theoretically described by [24]

$$A(t_i) = A(t_0)\frac{\sqrt{t_0}}{\sqrt{t_i}} \tag{1}$$

as shown in Fig. 10(a), where t_0 is the time that elapses when the elastic wave travels a reference distance with regard to the actuator and t_i is the moment when the signal is captured; $A(t_0)$ and $A(t_i)$ are the magnitudes of signals captured at moments t_0 and t_i, respectively.

To experimentally quantify the attenuation, five PZT wafers were surface-mounted in a straight line on an aluminium plate ($600 \times 600 \times 1.5$ mm^3) of all fixed edges, with the first one being the wave actuator and the rest being sensors (Sensors I/II/III/IV which were 100/200/320/480 mm away from the actuator, respectively). The A_0 modes captured by four sensors are combined in Fig. 10(b). The attenuation characteristics of the A_0 mode experimentally obtained are observed to be consistent with those from theoretical derivation described by Eq. (1). Based on this, attenuation of the A_0 mode with propagation distance was compensated in what follows using

$$f'(t) = f(t)\frac{\sqrt{d}}{\sqrt{d_0}}, \tag{2}$$

where $f(t)$ and $f'(t)$ are the captured and compensated wave signals, respectively; d is the propagation distance at which the wave signal is captured; and d_0 is a reference distance (e.g., 100 mm in this study). With Eq. (2), the magnitude of an experimentally acquired signal after travelling an arbitrary distance d becomes the same as that of a signal travelling a reference distance d_0 only (i.e., there were no further attenuation in magnitude between propagation distance $d-d_0$). Upon compensation, changes in signal intensity, if any, can be deemed as the sole consequence of diversity in damage orientation.

4. Probability-based diagnostic imaging

It is desirable to visualise structural damage in an intuitive image, and such an endeavour is generally named *diagnostic imaging*, exemplified by tomography [25,26] and migration techniques [27,28]. In these well-defined imaging techniques and tomography in particular, to reconstruct an image is often at the expense of using a large number of sensors. Aimed at circumventing such a deficiency, probability-based diagnostic imaging has been developed with the assistance of efficient information fusion algorithms, by taking full advantage of active sensor networks comprised of only a few sensors [29–32].

4.1. ToF-based field value

In a probability image, field values at pixels can be calculated using various signal features extracted from captured signals (e.g., ToF, signal magnitude and signal energy). In particular, ToF, the time consumed for a wave to travel a certain distance [20], is one of the most straightforward features of a wave signal, and was used for defining the field value in this
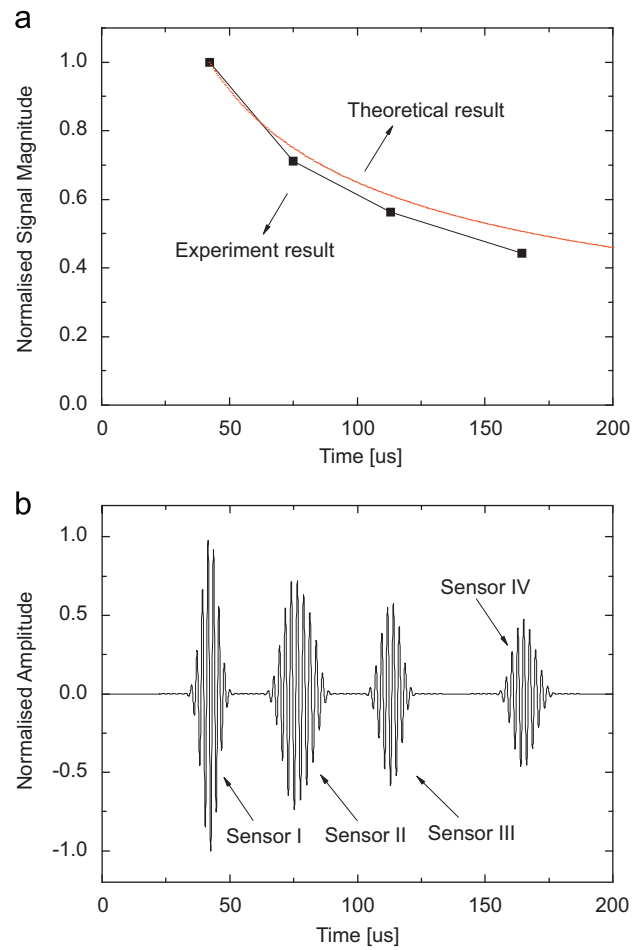
Fig. 10. (a) Wave attenuation trends obtained theoretically using Eq. (1) and measured experimentally and (b) combined A_0 modes in an aluminium plate of 1.5 mm in thickness captured by Sensors I/II/III/IV, 100/200/320/480 mm away from the actuator (normalised by the magnitude of signal captured by Sensor I).
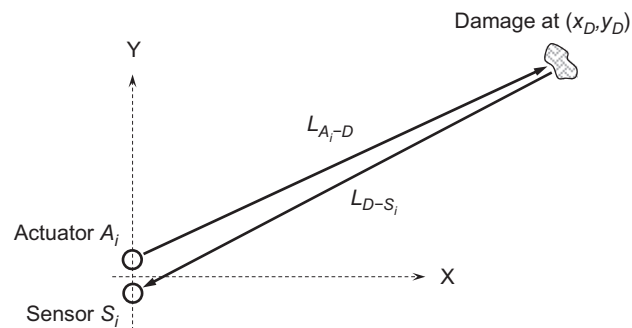

Fig. 11. Relative positions among actuator A_i, sensor S_i and damage in the local coordinate system for sensing path A_i-S_i.

approach. To brief the principle, consider a PZT sensor network consisting of N pulse–echo pairs (A_i-S_i ($i=1,2,\ldots,N$)). Without losing the generality, focusing on a pulse–echo path, A_i-S_i, a local coordinate system can be established for this path as shown in Fig. 11 schematically, where the system origin is at the midpoint between A_i and S_i, and the damage is presumed to be at (x_D,y_D) (two unknown variables to be determined). With the assumption that wave propagation velocity V is constant before and after interacting with damage (a more general scenario in which the velocity of damage-scattered wave is different from that of incident wave due to mode conversion can be referred to the authors' work reported

elsewhere [20]), a series of equations can be established for individual pulse–echo paths in the sensor network, as

$$\frac{L_{A_i-D}+L_{D-S_i}}{V}=\Delta t_i \quad (i=1,2,\ldots,N),\tag{3}$$

where Δt_i is the sum of (i) the ToF for the incident wave to propagate from A_i to the damage and (ii) the ToF for the damage-reflected wave to propagate from damage to S_i. L_{A_i-D} and L_{D-S_i} represent the distances between A_i and damage at (x_D,y_D), and the damage and S_i, respectively. Because the distance between A_i and S_i is much smaller than L_{A_i-D} and L_{D-S_i}, it can be hypothesised that $L_{A_i-D}=L_{D-S_i}=\sqrt{x_D^2+y_D^2}$. Mathematically, Eq. (3) depicts a circle-like locus which is the prior perception regarding the presence of damage from the perspective of the pulse–echo path that creates such a locus.

Subsequently, the structure under inspection, to which the above active sensor network is attached, is meshed using $L \times K$ nodes virtually (each mesh node is exclusively corresponding to a pixel of the probability image). At every single
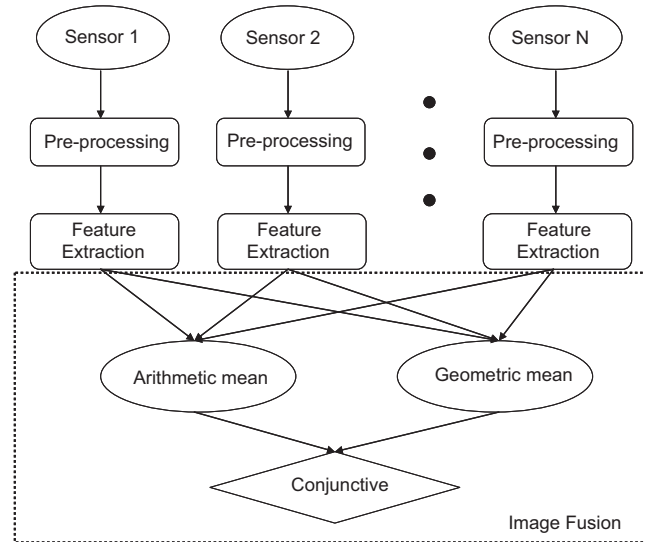

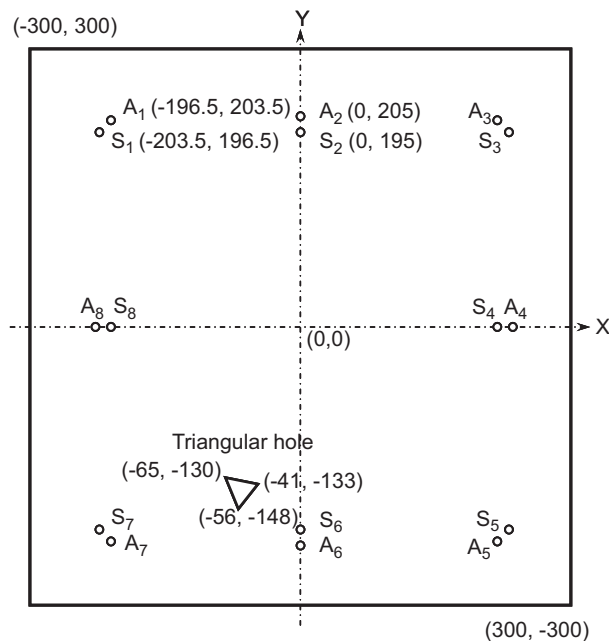Fig. 12. Flowchart of the two-level synthetic image fusion scheme.

Fig. 13. Specimen and sensor network configurations for identifying a triangular through-thickness damage (unit: mm) (allocation of PZT elements in the sensor network being symmetric relative to x and y axes).

mesh node, probabilities concerning damage presence perceived by individual sensing paths can be quantified in terms of the loci attained using Eq. (3): in principle, the nodes that rightly locate on a particular locus have the highest degree of probability (100%) of damage presence from the perspective of the sensing path that produces such a locus; for other
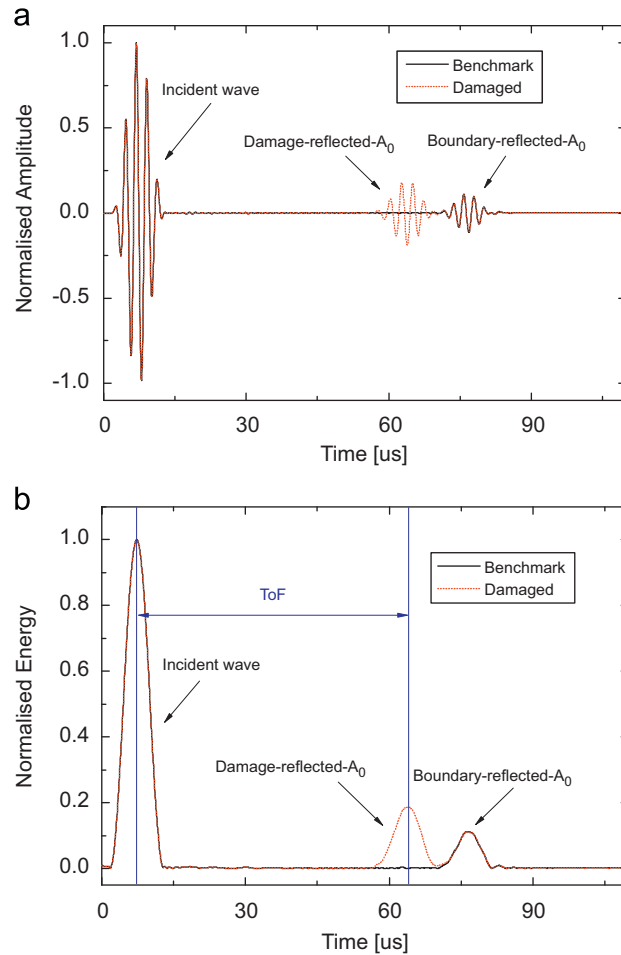

Fig. 14. (a) Lamb wave signals acquired via sensing path A_6-S_6 from FE simulation and (b) envelopes of energy distribution of signals in (a) obtained using HT-based signal processing (normalised by the magnitude of incident waves).
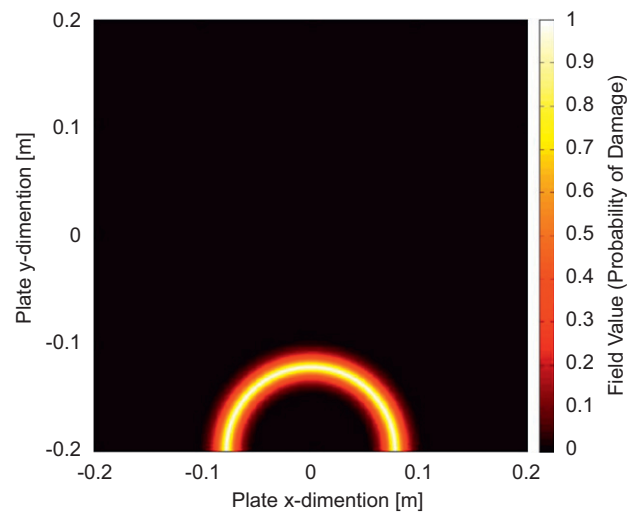

Fig. 15. Probability image established by sensing path A_6-S_6 (diagram showing inspection area only covered by the sensor network).

nodes, the further the distance to this locus, the less the probability the sensing path believes there is damage at those nodes. Therefore, the distance from a particular mesh node to the loci obtained by Eq. (3) can be associated with the probability of damage at this node. In the approach, a *cumulative distribution function* (CDF), $F(z)$, was introduced to facilitate the above procedure of defining field value, defined as

$$F(z) = \int_{-\infty}^{z} f(z_i) \, dz_i, \tag{4}$$

where

$$f(z_i) = \frac{1}{\sigma_i \sqrt{2\pi}} \exp\left[-\frac{z_i^2}{2\sigma_i^2}\right]$$

is the *Gaussian distribution function*, representing the probability density of damage presence at mesh node (x_m, y_n) $(m = 1, 2, \ldots, L;\ n = 1, 2, \ldots, K)$ established by sensing path $A_i - S_i \cdot z_i = \sqrt{(\overline{x}_i - x_m)^2 + (\overline{y}_i - y_n)^2}$, where $(\overline{x}_i, \overline{y}_i)$ is the location on the locus established by $A_i - S_i$ that has the shortest distance to (x_m, y_n). σ_i is the standard variance. Thus the field value at node (x_m, y_n) (i.e., the probability of damage presence at the point of the structure corresponding to (x_m, y_n)), $I(x_m, y_n)$, perceived by sensing path $A_i - S_i$ is

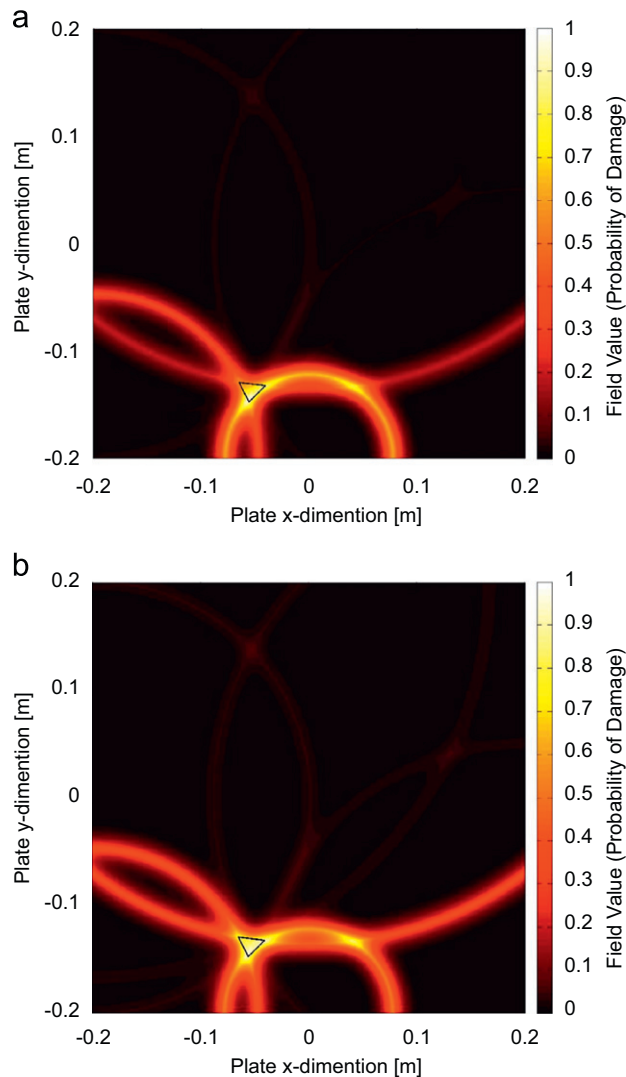$$I(x_m, y_n) = 1 - [F(z_i) - F(-z_i)]. \tag{5}$$

Fig. 16. Interim probability images obtained using arithmetic mean at the first level fusion: (a) without and (b) with compensation for wave attenuation as propagation distance.

4.2. Retrofitted field value by integrating intensity of signal energy

However, it is debatable whether ToF-based signal features are sufficient to deliver a quantitative depiction of damage including its orientation, shape and severity. That is because difference in damage orientation, shape and severity often impacts recognisable modulation on signal intensity, rather than ToF. As demonstrated in Section 2, the intensity of damage-reflected wave energy can be a sensitive indicator to damage orientation, based on which a retrofitted field value was proposed in the approach as

$$I(x_m,y_n)' = \frac{I(x_m,y_n) \times \Xi}{\Xi_{\max}},$$ (6)

where

$$\Xi = \xi \times \sqrt{t_{arr}}.$$

$I(x_m,y_n)$ is the field value at pixel (x_m,y_n) defined in terms of Eq. (5); $I(x_m,y_n)'$ is the retrofitted field value; ξ is the intensity of damage-reflected wave energy, subject to damage orientation as described in Figs. 4 and 8; $\sqrt{t_{arr}}$ is a factor to compensate for wave attenuation with propagation distance in terms of Eq. (2), where t_{arr} is the arrival time of the damage-reflected wave; and $\Xi_{\max}$ is the extremum of all captured Ξ. Integrating (i) intensity of damage-reflected wave energy (subject to damage orientation upon compensation for wave attenuation) with (ii) ToF (subject to location of damage), the retrofitted field value defined by Eq. (6) is endowed with an enhancive capacity to portray damage quantitatively including the orientation of its individual edges, whereby damage shape can further be ascertained if the damage is deemed as the continuum of a series of cracks with various lengths.

4.3. Imaging fusion scheme

Based on Eq. (6) each actuator–sensor pair of the active sensor network contributes a probability image, called *source image*. Source images contain, however, not only damage-scattered information but unwanted features such as measurement noise and uncertainties, multiple wave modes, reflections from structural boundaries, etc., presenting complexity in image appearance. To screen unwanted features and strengthen damage-associated information, a two-level synthetic image fusion scheme was developed. Image fusion, appropriately aggregating source images at the pixel-level leading to a resultant image, is a route from perceptions of individual sensing paths to ultimate consensus of the entire sensor network. Considering a sensor network consisting of N sensors, S_j $(j = 1,2,\ldots,N)$, each sensor independently perceives a damage event with a probability of E, defined by $P(E|S_j)$. The entire sensor network contributes in total N source images. In the proposed two-level fusion scheme, arithmetic mean and geometric mean were first applied to fuse all available source images, respectively, to obtain two interim images, in accordance with

$$arithmetic\,mean\,scheme : P_{arithmetic}(S_1,S_2,\ldots,S_N) = \frac{1}{N}\sum_{j=1}^{N} P(E|S_j),$$ (7a)

$$geometric\,mean\,scheme : P_{geometric}(S_1,S_2,\ldots,S_N) = \left(\prod_{j=1}^{N} P(E|S_j)\right)^{1/N}$$ (7b)
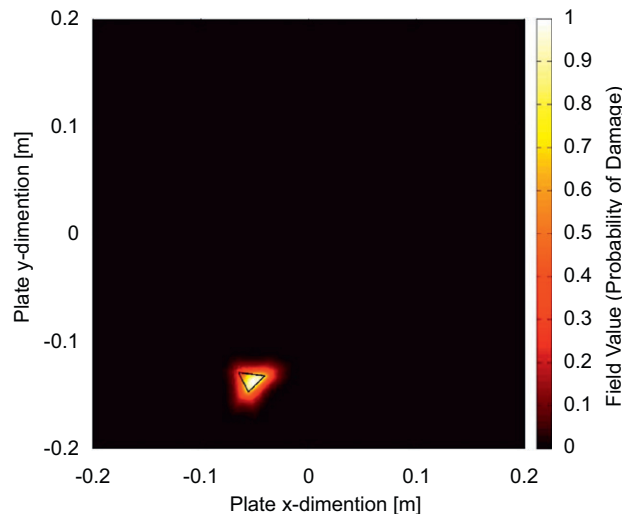

Fig. 17. Ultimate resultant image obtained using the two-level synthetic fusion scheme.

Subsequently, a conjunctive fusion technique [20] was applied to two interim images to obtain an ultimate resultant image, which is defined as

$$P_{conjunctive}(S_1,S_2,\ldots,S_N) = P_{arithmetic}(S_1,S_2,\ldots,S_N) \cap P_{geometric}(S_1,S_2,\ldots,S_N)$$
$$= P_{arithmetic}(S_1,S_2,\ldots,S_N) \cdot P_{geometric}(S_1,S_2,\ldots,S_N). \tag{8}$$

The conjunctive fusion aggregates two interim perceptions to strengthen a common part in between. As flowcharted in Fig. 12, such a synthetic fusion process stands out salient features of individual source images originated from damage and simultaneously suppresses less salient features in interim images such as measurement
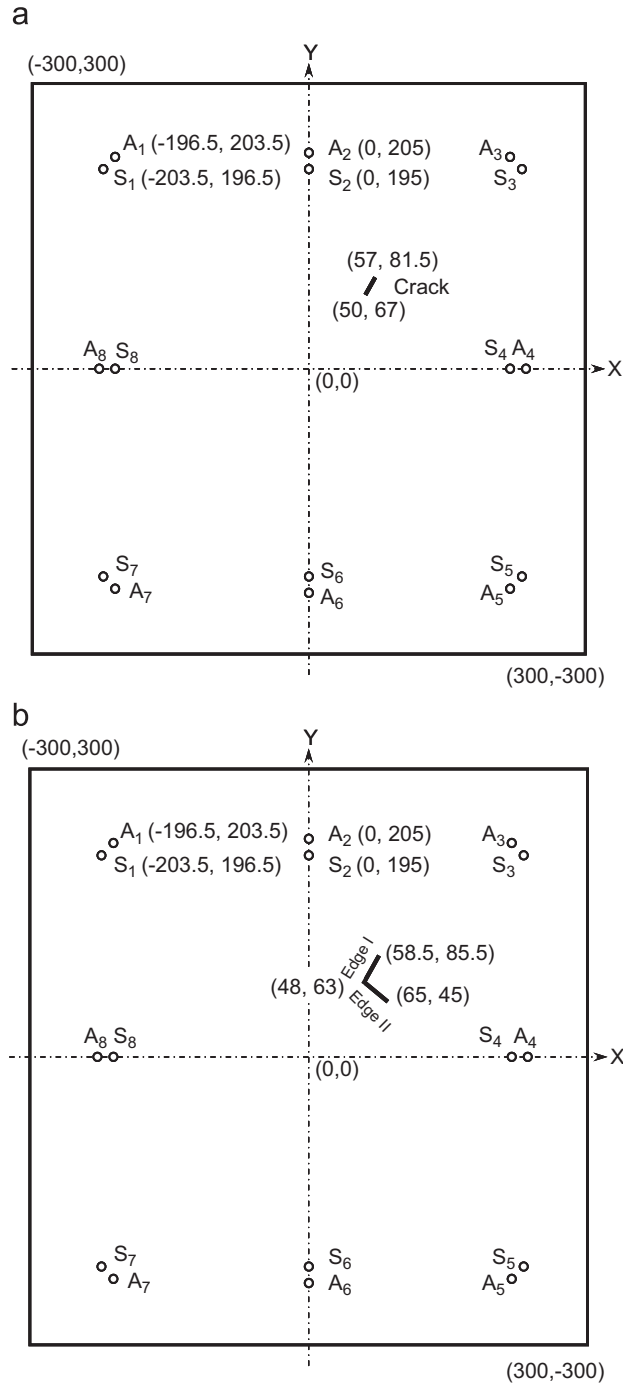

Fig. 18. Specimen and sensor network configurations for identifying (a) a through-thickness crack (Scenario I) and (b) an L-shape crack (Scenario II) (unit: mm) (allocation of PZT elements in the sensor network being symmetric relative to x and y axes).

noise and uncertainties. The motivation to develop such a synthetic fusion scheme is to reap merits of different fusion schemes for maximising fusion efficiency. The arithmetic mean is able to highlight prominence of damage-induced features in source images. However with increase of involved sensing paths (i.e., more source images) such prominence can be weakened considerably because each sensing path is only sensitive to the damage near it and contributes little to perceiving damage that is relatively far away from it (due to the use of exponential function in Eq. (5) for defining the field value). As a result, all source images are equally balanced, and the damage, highlighted in the images contributed by only few sensing paths near the damage, becomes de-emphasised in the ultimate resultant image. In contrast, the geometric mean possesses capability of de-noising since it highlights features in common only. But it might 'optimistically shrink' the likelihood of damage presence because such a fusion scheme multiplicatively processes all sources, and any low possibility in a particular source can lead to significantly low likelihood in the ultimate resultant image. The synthetic fusion exploits merits of arithmetic mean and geometric mean, so as to achieve a compromise in between, by equally taking into account all perceptions and well decentralising their contributions.

5. Damage identification using developed approach

5.1. Feasibility study using FE simulation

To demonstrate the effectiveness of the proposed approach for identifying orientation-specific damage, an aluminium plate ($600 \times 600 \times 1.5$ mm^3 with encastre boundary conditions) was considered, bearing a triangular through-thickness hole (the three edges are 20, 21 and 24 mm long, respectively), as shown in Fig. 13. The figure also shows a PZT sensor network, offering eight pulse–echo sensing pairs, A_i–S_i ($i = 1,2,\ldots,8$), in which A_i is 10 mm apart from S_i. The aluminium plate and PZT elements were modelled in ABAQUS®/EXPLICIT using the same modelling and simulation technique introduced in Section 2.1. The triangular damage was formed by removing associated FE elements. *Hanning*-window-modulated five-cycle sinusoidal tonebursts at a central frequency of 450 kHz were applied on FE nodes of the upper and lower surfaces of each PZT actuator model in the out-of-plane direction to generate the A_0 mode dominating overall signal energy. The damage-scattered wave signals were captured by calculating the strains at places where eight sensors were located.

As a representative example, the Lamb wave signal captured via sensing path A_6–S_6, after being normalised by the magnitude of the incident wave, is displayed in Fig. 14(a). For comparison, the corresponding baseline signal is also
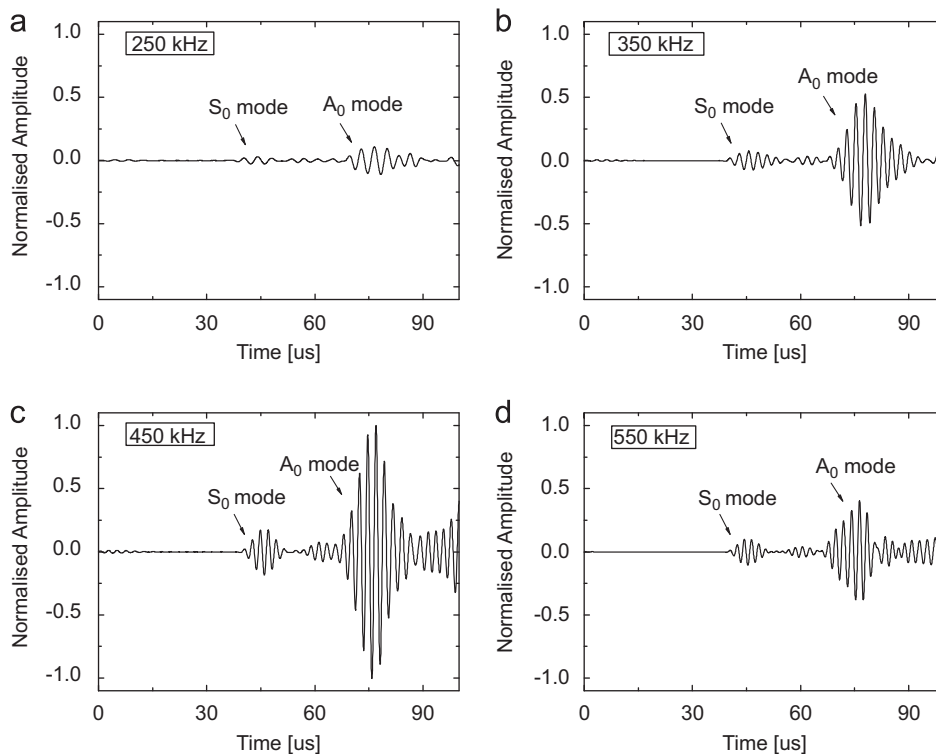

Fig. 19. Lamb wave signals acquired via sensing path A_5–S_4 at excitation frequencies of (a) 250 kHz, (b) 350 kHz, (c) 450 kHz and (d) 550 kHz (normalised by the magnitude of signal at 450 kHz).

presented, where the damage-reflected A_0 mode stands out clearly. As a result of small angle of wave incidence offered by path A_6–S_6 ($\theta < 5^0$), the damage-reflected A_0 can be seen strong in magnitude, coinciding with observations in Figs. 4 and 8. The signal was subsequently treated with HT-based signal processing, Fig. 14(b), from which ToF and intensity of damage-reflected wave energy were extracted. The probability image for this sensing path was accordingly established using Eq. (6), shown in Fig. 15.

Source images contributed by eight sensing paths of the sensor network using the above process were fused with the two-level synthetic image fusion scheme. The interim images obtained using the arithmetic mean at the first level fusion, without and with compensation for wave attenuation, are displayed in Fig. 16. Without the compensation, the approach fails to predict the damage accurately (Fig. 16(a)), because reduction in intensity of wave energy as propagation distance was counted by the algorithm as changes in damage orientation. Note that no pronounced error in predicting damage location can be noticed even without such compensation, because prediction of damage location by this algorithm is fully based on ToFs in terms of Eq. (5), independent of signal intensity. In the contrast, both location and shape of the damage can be estimated accurately when compensation was applied, Fig. 16(b). Further applying the second level fusion on interim images, the ultimate resultant probability image is exhibited in Fig. 17, where orientation of three individual edges of the triangular damage are revealed clearly, facilitating description of damage shape.

5.2. Parametric study using experiment

5.2.1. Experiment set-up and signal processing

An aluminium sample same as the one used in the above was prepared. A through-thickness crack of 16 mm in length and 0.64 mm in width (Scenario I) was introduced to the plate using a fine blade. The crack was then extended to an
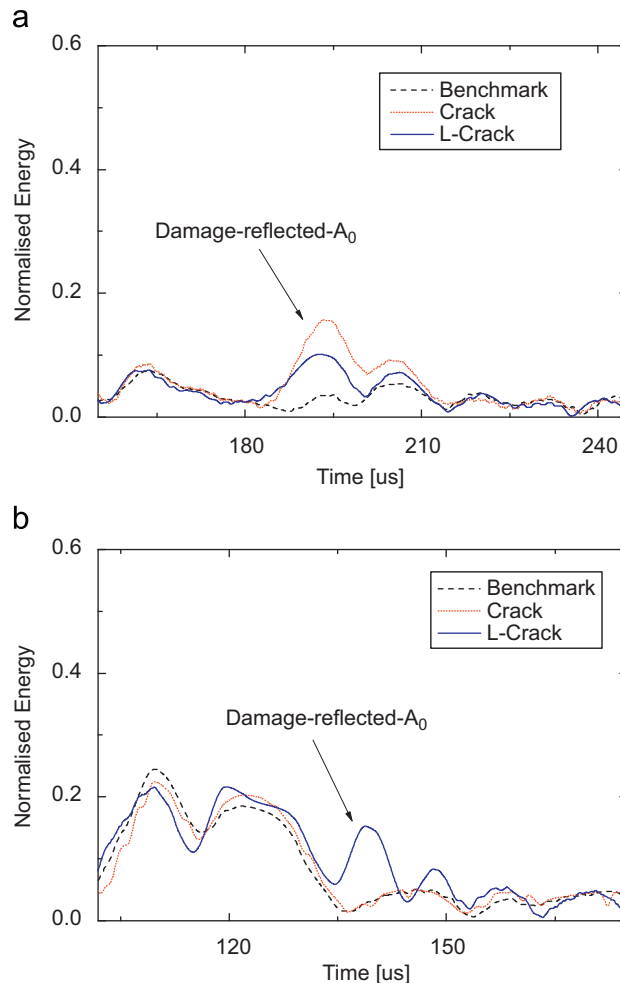

Fig. 20. Envelopes of energy distribution of Lamb wave signals acquired via (a) A_1–S_1 and (b) A_3–S_3 (both from experiment) for two damage scenarios (showing signal fragments containing damage-reflected A_0 mode only; normalised by the magnitude of corresponding incident waves).

L-shape crack consisting of two through-thickness cracks (Edges I and II), 25 mm long and 1.5 mm wide each (Scenario II). Two damage scenarios are shown schematically in Fig. 18(a) and (b), respectively. An active sensor network consisting of 16 circular PZT wafers with properties in Table 1 was surface-mounted to the plate to configure eight pulse–echo sensing pairs. The signal generation and acquisition system introduced in Section 2.2 was recalled to produce five-cycle *Hanning*-window-modulated sinusoid tonebursts which were then applied in turn on each PZT actuator to generate the A_0 mode dominantly after being amplified to 60 V_{p-p}. The crack-reflected wave signals were acquired via eight pulse–echo paths. In experiment it is important to get aware of the most appropriate frequency at which the activated waves are able to deliver the maximum coupling between the host structure and PZT wafers, leading to a high SNR. To determine such a frequency, a sweep frequency test from 200 to 700 kHz was conducted. The Lamb wave signal acquired via sensing path A_5-S_4 at frequencies of 250, 350, 450 and 550 kHz, as examples, are compared in Fig. 19, to observe that the wave signal at a central frequency of 450 kHz presents the maximum response in signal magnitude. Accordingly, 450 kHz was selected as the excitation frequency in all following experiments.

Representatively, HT-processed signals acquired via path A_1-S_1 and A_3-S_3 are displayed in Fig. 20(a) and (b) for two damage scenarios, respectively. All captured signals were normalised relative to the magnitude of their corresponding incident waves, respectively, prior to HT. This process was aimed to eliminate discrepancy of soldering and bonding among different actuator–sensor pairs. In Fig. 20(a) for A_1-S_1, A_0 modes reflected by the crack (Scenario I) and the L-shape crack (Scenario II) are high in intensity, because of the relatively small angle of wave incidence ($\theta < 5^0$) with regard to the orientation of crack (in Scenario I) and orientation of Edge I (in Scenario II). In Fig. 20(b) for A_3-S_3, strong reflection remains for Scenario II but not for Scenario I, and that is because the angle of wave incidence via this sensing path is large ($\theta > 70^0$) with regard to the orientation of crack (in Scenario I), leading to weak scattering in terms of Figs. 4 and 8. For Scenario II,
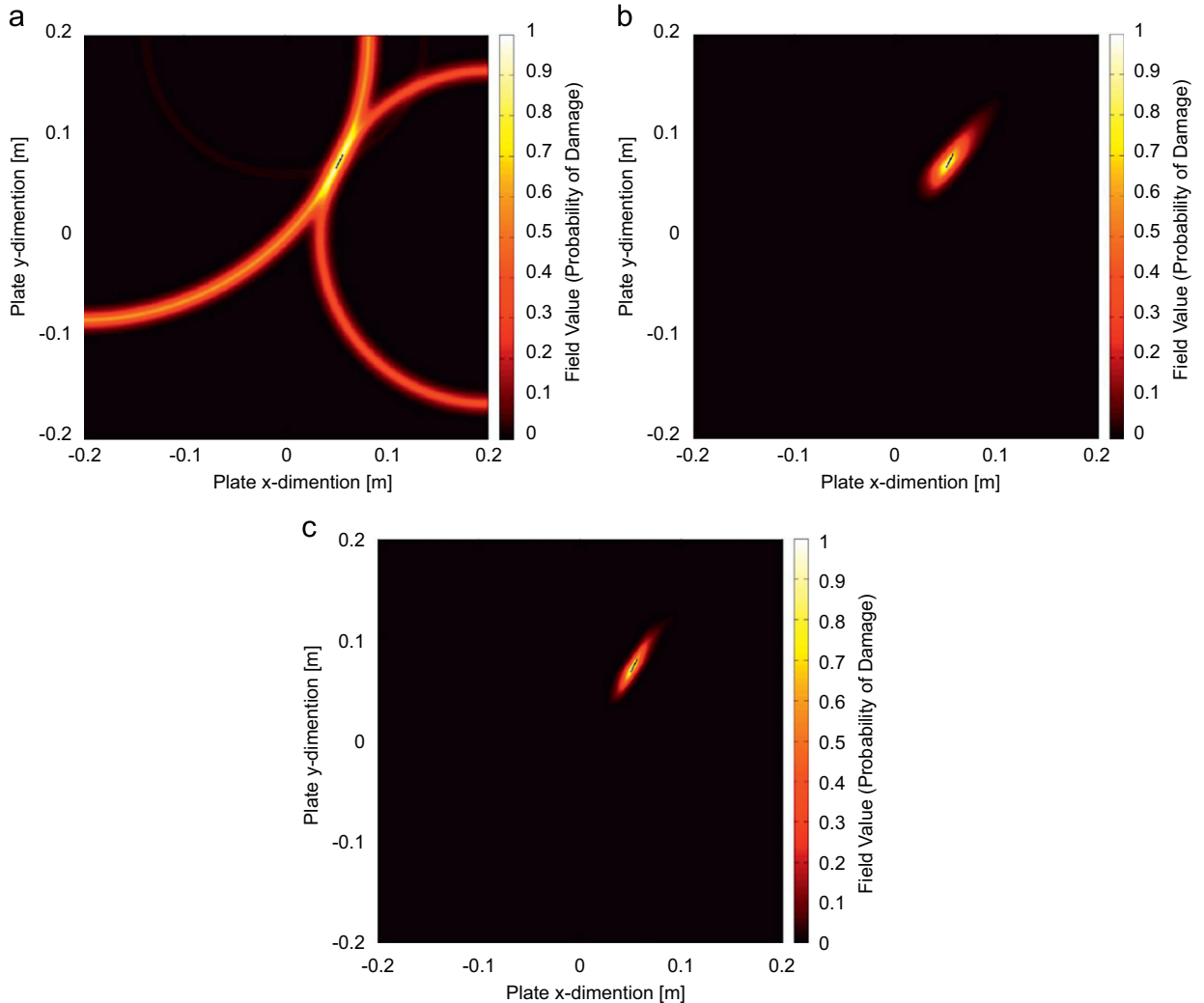

Fig. 21. Probability images for Scenario I using (a) arithmetic mean (interim image), (b) geometric mean (interim image) at the first level and (c) conjunctive fusion (ultimate image) at the second level (short solid line: real crack).
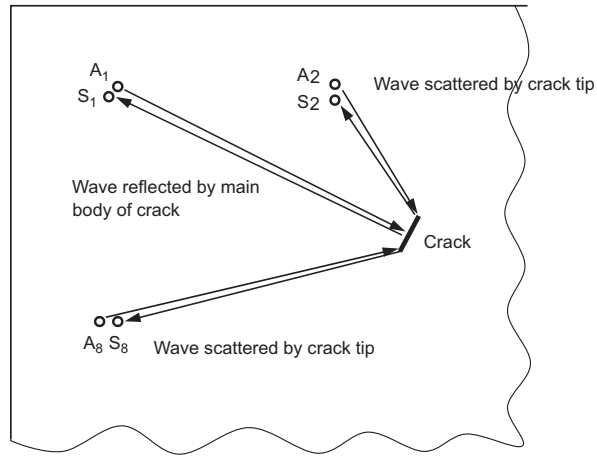
Fig. 22. Illustration for signal feature extraction via different sensing paths in a sensor network (different sensing paths providing various signal features associated with damage for two-level synthetic image fusion).
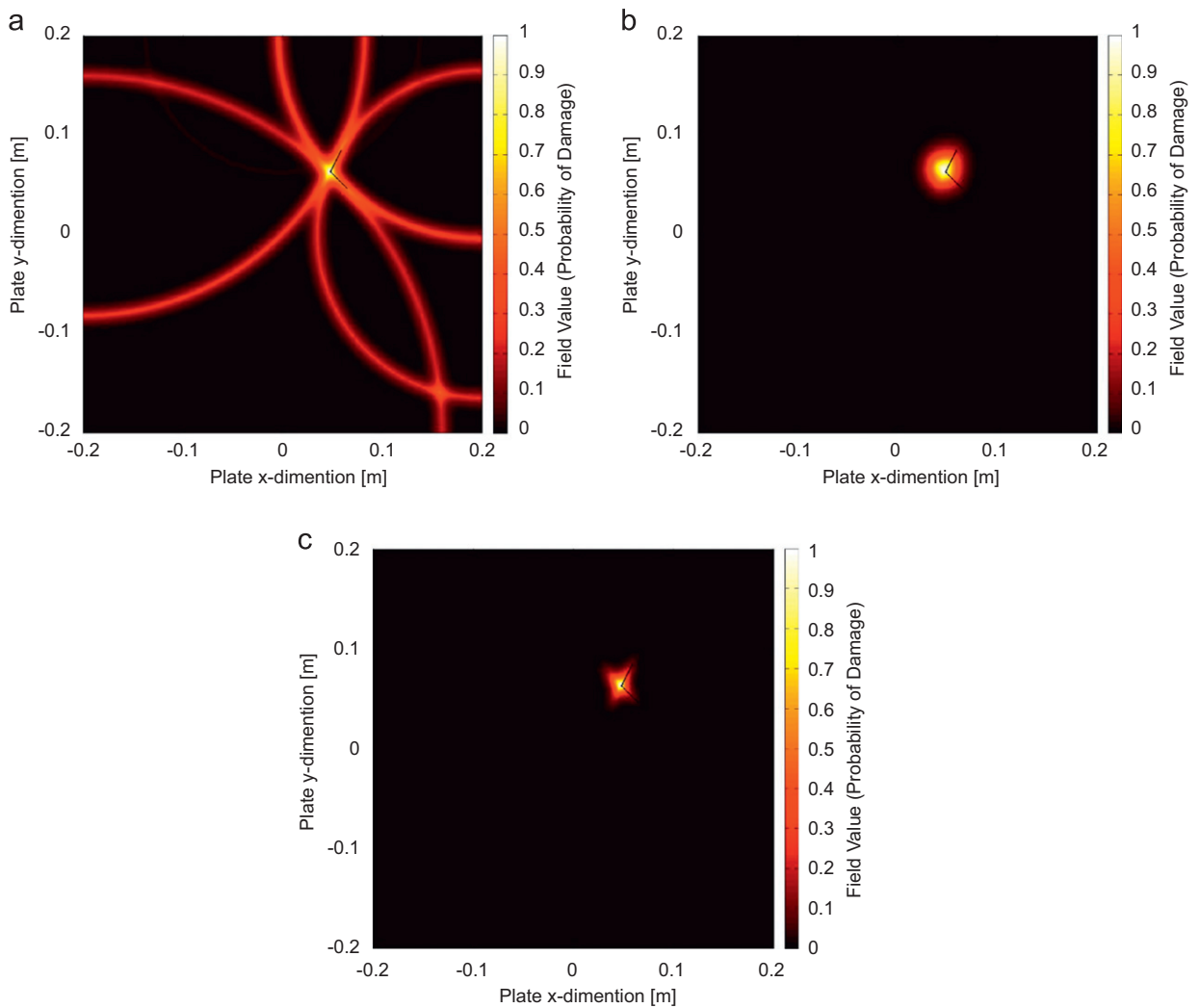

Fig. 23. Probability images for Scenario II using (a) arithmetic mean (interim image), (b) geometric mean (interim image) at the first level and (c) conjunctive fusion (ultimate image) at the second level (short solid line: real edge of L-shape crack).

incident wave via A_3-S_3 becomes insensitive to Edge I, but it is well scattered by Edge II ($\theta < 5^0$), therefore keeping a high intensity.

5.2.2. Identification results and discussion

Applying the developed imaging approach supplemented with the two-level synthetic fusion scheme, two interim and ultimate resultant images for Scenario I are shown in Fig. 21, to observe accurate identification results in the ultimate resultant image (Fig. 21(c)), in which the predicted damage location, orientation and length match well the real ones.

It is noteworthy that in this approach both the waves reflected from the main body of crack and the waves scattered from crack tips were taken into account, thanks to the active sensor network which enabled the diagnostic waves to be emitted from different incidence angles, as explained in Fig. 22 for Scenario I, where the waves reflected by the main body of crack were captured by sensing path A_1-S_1 while waves scattered by individual crack tips by A_2-S_2 and A_8-S_8, respectively. Features extracted from signals captured via different paths were then fused using the two-level synthetic image fusion. This makes it possible to deliver a quantitative description of the damage including the orientation and size.

For Scenario II, the interim and ultimate resultant images are shown in Fig. 23. Relatively large prediction errors are observed, which are attributable to the fact that Edges I and II are almost perpendicular to each other, and if a particular sensing path perceives strong reflection from one of the two edges then the same sensing path would be insensitive to the other; when all images are fused, the common part perceived by this sensing path (connection area of Edges I and II) is double enhanced in the ultimate resultant image, but two tips of the L-shape crack are de-emphasised. For this reason, two
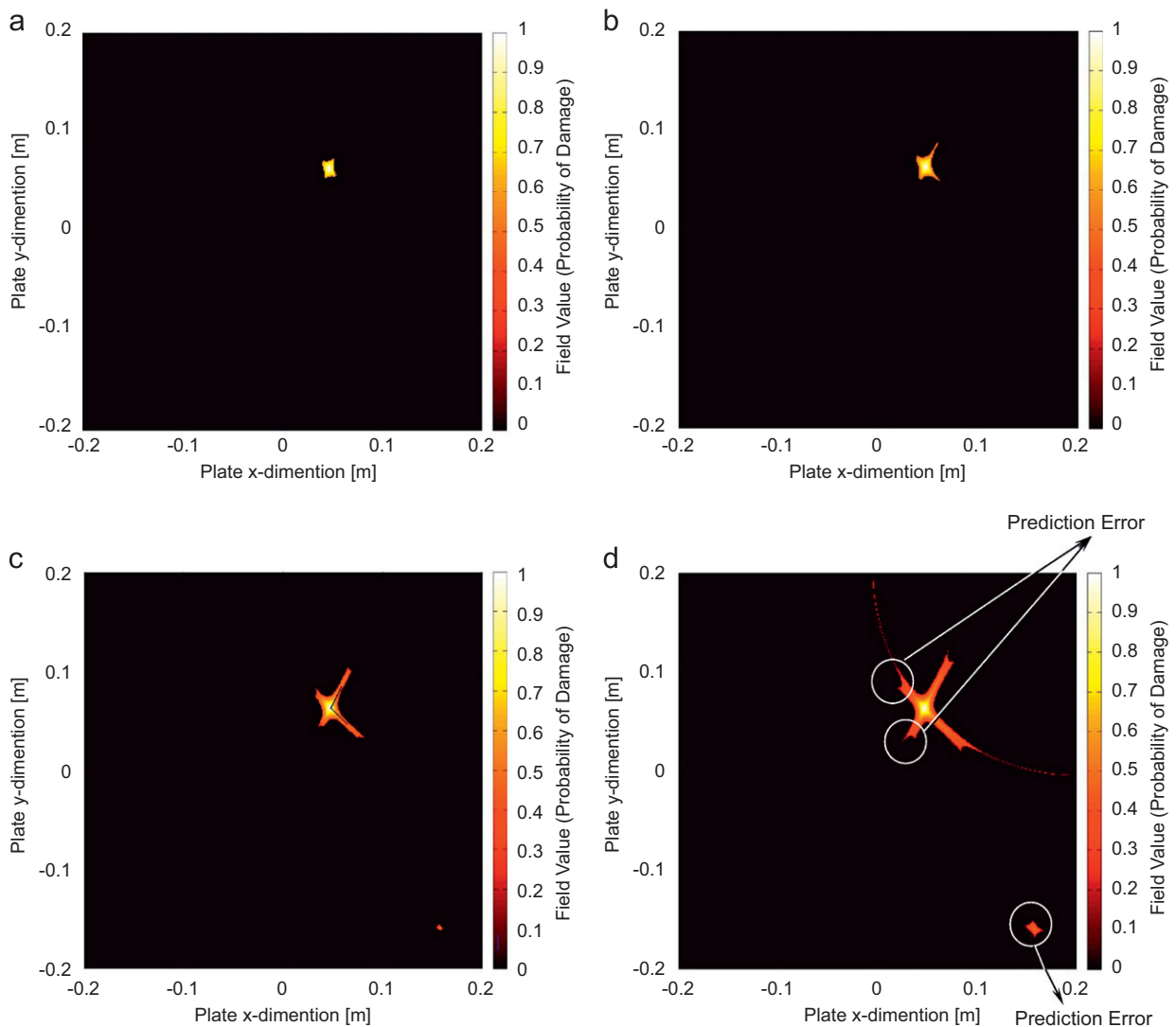

Fig. 24. Ultimate resultant image for Scenario II obtained by applying different field value thresholds during the arithmetic mean at the first level fusion: (a) 0.6, (b) 0.5, (c) 0.4 and (d) 0.3.

edges of the L-shape crack are not clearly highlighted simultaneously in the resultant image. Although this might not be a problematic issue if an active sensor network with sufficient actuators and sensors is used, a threshold-based enhancement was further introduced in the approach. The threshold, κ, is a preset percentage of the maximum field value, $I(x_m, y_n)'$, of the ultimate probability image, and any field value defined by Eq. (6) less than such a threshold is set to be zero during the arithmetic mean, and otherwise remained. Shown in Fig. 24 are probability images upon applying several thresholds ($\kappa = 0.6$, 0.5, 0.4, 0.3, respectively) for Scenario II. It can be seen that, with the decrease of κ (from 0.6 down to 0.3), the shape of L-shape crack becomes obvious. That is because more perceptions concerning damage from various sensing paths are accentuated in the ultimate image at a smaller threshold. But when the threshold is excessively small (e.g., $\kappa = 0.3$), measurement noise tends to appear, masking the actual shape of damage and leading to erroneous prediction as seen in Fig. 24(d).

To further examine the dependence of sensitivity of the approach on the number of pulse–echo sensing paths involved for image fusion, the sensor network configuration in Scenario II was changed by abandoning sensing paths A_8–S_8 and A_1–S_1, respectively (i.e., de-activating A_8 and A_1, respectively). For the former case (de-activating A_8), two edges of the L-shape crack can still be highlighted clearly in the ultimate resultant image, in Fig. 25(a), matching well the actual one; whereas, for the latter (de-activating A_1), Edge I could not be identified any more in the ultimate resultant image, in Fig. 25(b). This is due to the fact (from the conclusions of the preliminary study detailed in Section 2) that each orientation-specific damage holds a sensitive region in which the angle of wave incidence (θ in Fig. 1) is sufficiently small so as to ensure the damage-reflected wave energy to be captured efficiently. According to Figs. 4 and 8, the sensitive
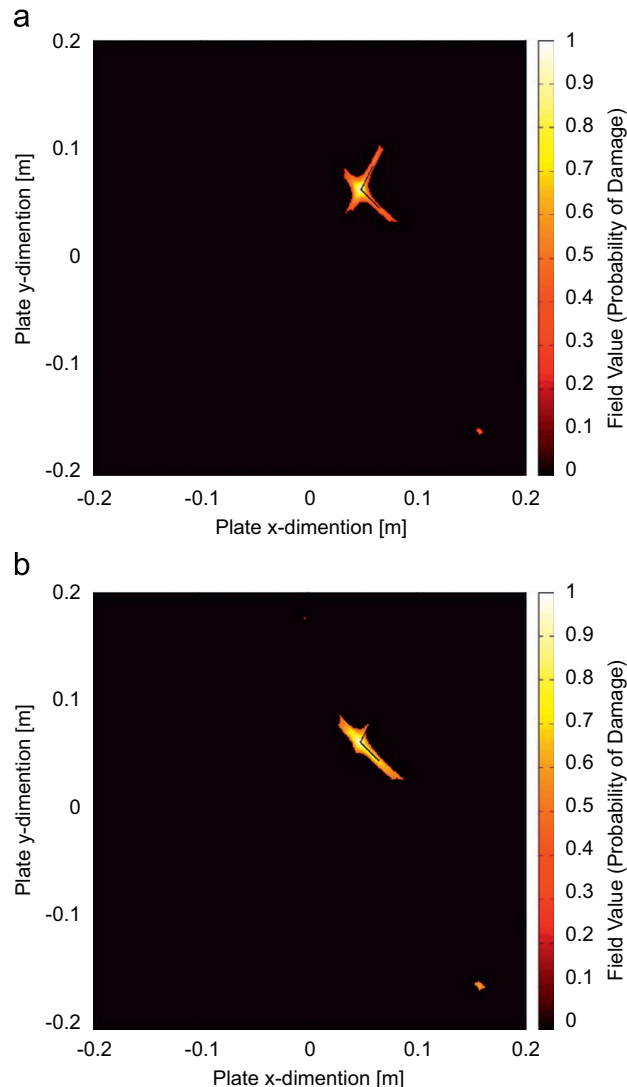

Fig. 25. Ultimate resultant image for Scenario II obtained by abandoning (a) sensing path A_8–S_8 (de-activating A_8) and (b) A_1–S_1 (de-activating A_1) in the sensor network.
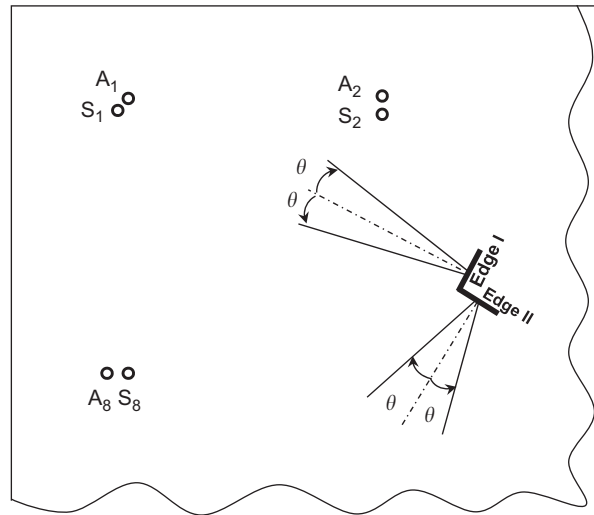
Fig. 26. Sensitive regions of Edges I and II in Scenario II.

regions for Edges I and II are indicated in Fig. 26. Since A_1-S_1 right passes through the sensitive region of Edge I, loss of this path makes Edge I unable to be identified; whereas, A_8-S_8 is away from the sensitive region of any edge, and absence of this sensing path would not influence the description of the damage prominently.

6. Conclusion

In recognition of the deficiencies of most approaches using elastic waves for quantitatively identifying orientation-specific damage such as a crack or a notch, intensity of crack-scattered wave signal energy subject to different angles of wave incidence was investigated and calibrated, which was integrated with temporal information extracted from captured wave signals. Based on this, a retrofitted probability-based diagnostic imaging approach was developed, in conjunction with use of an active sensor network in a pulse–echo configuration. Damage location, orientation of individual edges and therefore the shape of the damage can be estimated quantitatively. To enhance robustness and tolerance to measurement noise/uncertainties and possible erroneous perceptions from particular sensing paths, a two-level synthetic image fusion scheme was introduced. The effectiveness of this approach was demonstrated by predicting orientation-specific damage including a triangular through-thickness hole (through FE simulation), a through-thickness crack and an L-shape crack (through experiment) in aluminium plates. The results, highlighted in intuitional and easily interpretable images, have shown satisfactory accuracy of the developed approach for identifying orientation-specific damage.

Acknowledgement

References

[1] J. Grabowska, M. Palacz, M. Krawczuk, Damage identification by wavelet analysis, Mechanical Systems and Signal Processing 22 (2008) 1623–1635.
[2] S.S. Kessler, S.M. Spearing, C. Soutis, Damage detection in composite materials using Lamb wave methods, Smart Materials and Structures 11 (2002) 269–278.
[3] M.B. Lemistre, D.L. Balageas, A hybrid electromagnetic acousto-ultrasonic method for SHM of carbon/epoxy structures, Structural Health Monitoring—an International Journal 2 (2003) 153–160.
[4] W.J. Staszewski, C. Boller, G.R. Tomlinson, Health Monitoring of Aerospace Structures: Smart Sensor Technologies and Signal Processing, John Wiley & Sons, Inc., New York, USA, 2004.
[5] V. Giurgiutiu, Tuned Lamb wave excitation and detection with piezoelectric wafer active sensors for structural health monitoring, Journal of Intelligent Material Systems and Structures 16 (2005) 291–305.
[6] H.W. Park, H. Sohn, K.H. Law, C.R. Farrar, Time reversal active sensing for health monitoring of a composite plate, Journal of Sound and Vibration 302 (2007) 50–66.
[7] E.A. Birt, Application of ultrasonic Lamb waves for damage detection in carbon fibre composite aerospace structures, Insight 44 (2002) 423–427.
[8] J.D. Achenbach, Quantitative nondestructive evaluation, International Journal of Solids and Structures 37 (2000) 13–27.
[9] T. Kundu, S. Das, K.V. Jata, Health monitoring of a thermal protection system using Lamb waves, Structural Health Monitoring—an International Journal 8 (2009) 29–45.
[10] S.R. Anton, D.J. Inman, G. Park, Reference-free damage detection using instantaneous baseline measurements, AIAA Journal 47 (2009) 1952–1964.

[11] W. Ostachowicz, P. Kudela, P. Malinowski, T. Wandowski, Damage localisation in plate-like structures based on PZT sensors, Mechanical Systems and Signal Processing 23 (2009) 1805–1829.
[12] M.J.S. Lowe, P. Cawley, J.Y. Kao, O. Diligent, The low frequency reflection characteristics of the fundamental antisymmetric Lamb wave A_0 from a rectangular notch in a plate, Journal of the Acoustical Society of America 112 (2002) 2612–2622.
[13] M.J.S. Lowe, O. Diligent, Low-frequency reflection characteristics of the S_0 Lamb wave from a rectangular notch in a plate, Journal of the Acoustical Society of America 111 (2002) 64–74.
[14] J.-B. Ihn, F.-K. Chang, Detection and monitoring of hidden fatigue crack growth using a built-in piezoelectric sensor/actuator network: I. Diagnostics, Smart Materials and Structures 13 (2004) 609–620.
[15] P.S. Tua, S.T. Quek, Q. Wang, Detection of cracks in plates using piezo-actuated Lamb waves, Smart Materials and Structures 13 (2004) 643–660.
[16] Y. Lu, L. Ye, Z. Su, N. Huang, Quantitative evaluation of crack orientation in aluminium plates based on Lamb waves, Smart Materials and Structures 16 (2007) 1907–1914.
[17] Z.S. Chang, A. Mal, Scattering of Lamb waves from a rivet hole with edge cracks, Mechanics of Materials 31 (1999) 197–204.
[18] T.R. Hay, R.L. Royer, H. Gao, X. Zhao, J.L. Rose, A comparison of embedded sensor Lamb wave ultrasonic tomography approaches for material loss detection, Smart Materials and Structures 15 (2006) 946–951.
[19] X. Zhao, H. Gao, G. Zhang, B. Ayhan, F. Yan, C. Kwan, J.L. Rose, Active health monitoring of an aircraft wing with embedded piezoelectric sensor/actuator network: I. Defect detection, localization and growth monitoring, Smart Materials and Structures 16 (2007) 1208–1217.
[20] Z. Su, X. Wang, L. Cheng, L. Yu, Z. Chen, On selection of data fusion schemes for structural damage evaluation, Structural Health Monitoring—an International Journal 8 (2009) 223–241.
[21] A. Raghavan, C.E.S. Cesnik, Review of guided-wave structural health monitoring, The Shock and Vibration Digest 39 (2007) 91–114.
[22] N.E. Huang, Z. Shen, S.R. Long, M.L.C. Wu, H.H. Shih, Q.N. Zheng, N.C. Yen, C.C. Tung, H.H. Liu, The empirical mode decomposition and the Hilbert spectrum for nonlinear and non-stationary time series analysis, Proceedings of the Royal Society of London Series A—Mathematical Physical and Engineering Sciences 454 (1998) 903–995.
[23] Z. Su, L. Ye, Lamb wave propagation-based damage identification for quasi-isotropic CF/EP composite laminates using artificial neural algorithm, Part II: Implementation and validation, Journal of Intelligent Material Systems and Structures 16 (2005) 113–125.
[24] G. Konstantinidis, B.W. Drinkwater, P.D. Wilcox, The temperature stability of guided wave structural health monitoring systems, Smart Materials and Structures 15 (2006) 967–976.
[25] J.C.P. McKeon, M.K. Hinders, Parallel projection and crosshole Lamb wave contact scanning tomography, Journal of the Acoustical Society of America 106 (1999) 2568–2577.
[26] E.V. Malyarenko, M.K. Hinders, Fan beam and double crosshole Lamb wave tomography for mapping flaws in aging aircraft structures, Journal of the Acoustical Society of America 108 (2000) 1631–1639.
[27] L. Wang, F.G. Yuan, Damage identification in a composite plate using prestack reverse-time migration technique, Structural Health Monitoring—an International Journal 4 (2005) 195–211.
[28] X. Lin, F.G. Yuan, Experimental study applying a migration technique in structural health monitoring, Structural Health Monitoring—an International Journal 4 (2005) 341–353.
[29] C.H. Wang, J.T. Rose, F.-K. Chang, A synthetic time-reversal imaging method for structural health monitoring, Smart Materials and Structures 13 (2004) 415–423.
[30] J.E. Michaels, T.E. Michaels, Guided wave signal processing and image fusion for in situ damage localization in plates, Wave Motion 44 (2007) 482–492.
[31] J.-B. Ihn, F.-K. Chang, Pitch-catch active sensing methods in structural health monitoring for aircraft structures, Structural Health Monitoring—an International Journal 7 (2008) 5–19.
[32] G. Konstantinidis, P.D. Wilcox, B.W. Drinkwater, An investigation into the temperature stability of a guided wave structural health monitoring system using permanently attached sensors, IEEE Sensors Journal 7 (2007) 905–912.